

Performance of the Imaging Fourier Transform Spectrometer with Photoconductive Detector Arrays: An Application for the AKARI Far-Infrared Instrument

Mitsunobu KAWADA¹, Hidenori TAKAHASHI², Noriko MURAKAMI^{1,3}, Hiroshi MATSUO⁴, Yoko OKADA⁵, Akiko YASUDA⁵, Shuji MATSUURA⁵, Mai SHIRAHATA⁵, Yasuo DOI⁶, Hidehiro KANEDA⁵, Takafumi OOTSUBO⁵, Takao NAKAGAWA⁵, and Hiroshi SHIBAI^{1,7}

¹*Graduate School of Sciences, Nagoya University, Furo-cho, Chikusa-ku, Nagoya 464-8602, Japan
kawada@u.phys.nagoya-u.ac.jp*

²*Gunma Astronomical Observatory, 6860-86 Nakayama, Takayama, Agatsuma, Gunma 377-0702, Japan*

³*Bisei Astronomical Observatory, Okura, Bisei-cho, Ibara-shi, Okayama 714-1411, Japan*

⁴*Advanced Technology Center, National Astronomical Observatory of Japan, 2-21-1 Osawa, Mitaka, Tokyo 181-8588, Japan*

⁵*Institute of Space and Astronautical Science, JAXA, 3-1-1 Yoshinodai, Sagamihara 229-8510, Japan*

⁶*Department of General System Studies, Graduate School of Arts and Sciences, The University of Tokyo, 3-8-1 Komaba, Meguro-ku, Tokyo 153-8902, Japan*

⁷*Graduate School of Sciences, Osaka University, 1-1 Machikaneyama-cho, Toyonaka-shi, Osaka 560-0043, Japan*

(Received 2008 June 0; accepted 2008 0)

Abstract

We have developed an imaging Fourier transform spectrometer (FTS) for space-based far-infrared astronomical observations. The FTS employs a newly developed photoconductive detector arrays with a capacitive trans-impedance amplifier, which makes the FTS a completely unique instrument. The FTS was installed as a function of the far-infrared instrument (FIS: Far-Infrared Surveyor) on the Japanese astronomical satellite, AKARI, which was launched on February 21, 2006 (UT) from the Uchinoura Space Center. The FIS-FTS had been operated for more than one year before liquid helium ran out on August 26, 2007. The FIS-FTS was operated nearly six hundreds times, which corresponds to more than one hundred hours of astronomical observations and almost the same amount of time for calibrations. As expected from laboratory measurements, the FIS-FTS performed well and has produced a large set of astronomical data for valuable objects. Meanwhile, it becomes clear that the detector transient effect is a considerable factor for FTSs with photoconductive detectors. In this paper, the instrumentation of the FIS-FTS and interesting phenomena related to FTS using photoconductive detectors are described, and future applications of this kind of FTS system are discussed.

Key words: instrumentation:spectrographs — space vehicles:instruments — techniques:spectroscopic

1. Introduction

Observations using infrared wavelengths are progressing in many fields of science and technology. In astrophysics, space-based infrared astronomy has become a powerful tool for deep insights into the universe ever since the first astronomical satellite, IRAS, was launched in 1983 (Neugebauer et al. 1984). The earliest instruments for infrared astronomy were photometers using discrete detectors, and observations become gradually more precise, driven by the evolution of infrared technology. The development of detector arrays allowed detailed images to be recorded efficiently, and when coupled with spectrometers, provided detailed imaging spectroscopy. The COBE satellite (Mather 1993), which was launched in 1989, measured the precise spectra and absolute power of the cosmic infrared background radiation. IRTS (Murakami et al. 1996), which was launched in 1995 as the first Japanese infrared telescope in space, have mapped 7 % of the sky, and have provided near- (Tanaka et al. 1996), mid- (Onaka et

al. 1996), and far- (Shibai et al. 1996) infrared spectra and line intensities as well as sub-millimeter brightness distribution (Hirao et al. 1996). The ISO (Kessler et al. 1996; Kessler 2002), which was launched in 1995, provided a lot of infrared spectra for various objects, and emphasized the importance of studying infrared lines for investigations of the interstellar medium. The Spitzer Space Telescope (Werner et al. 2004), the infrared astronomical satellite launched in 2003, provides valuable images and spectra for various objects, but has only limited spectroscopic capabilities in the far infrared wavelength range.

The AKARI satellite (Murakami et al. 2007) is the Japanese infrared astronomical satellite, which was launched in 2006. AKARI has a 68.5 cm diameter cooled telescope (Kaneda et al. 2007) and two focal plane instruments; one is the IRC (InfraRed Camera) (Onaka et al. 2007) for near to mid infrared range and the other is the FIS (Far-Infrared Surveyor) (Kawada et al. 2007) for far-infrared imaging photometry. The FIS has spectroscopic capabilities as an optional function, provided by

a Fourier transform spectrometer (FTS) (Takahashi et al. 2003). The FTS of the FIS (hereafter FIS-FTS) is the second spectrometer for far-infrared astronomy operated in space after FIRAS (Mather et al. 1993) of the COBE satellite. A unique feature of the FIS-FTS is the imaging FTS design using a photoconductive detector system. The design, operation and performance of the FIS-FTS are described in this paper; the data reduction and the calibration of the FIS-FTS are treated in the companion paper (Murakami et al. 2008), and some scientific results related to the FIS-FTS are discussed by some authors (Yasuda et al. 2008; Okada et al. 2008; Takahashi et al. 2008). In the next section, the optical and mechanical design of the FIS-FTS are described. After explaining the operation of the FIS-FTS in section 3, the performance and some interesting properties of the FIS-FTS are presented in section 4. In section 5, we discuss special topics related to the FIS-FTS and future applications of FTSs with photoconductive detectors.

2. Instrumentation

2.1. Optical Design

The FIS-FTS adopts a polarized Michelson-type Martin-Puplett interferometer (MPI) design (Martin & Puplett 1969). MPIs require a linear polarized light for input, which is then divided into two polarization components by a polarizing beam splitter. The two components are interfered as an elliptically polarized beam according to the incident spectrum and the optical path difference between the two components. By picking up the polarization component parallel or perpendicular to the polarization angle of the incident beam, interferograms can be recorded.

A schematic view of the FIS-FTS optics is shown in figure 1. The photometer and the FTS are individually selected by rotating the filter wheel. The collimator and camera optics, some optical filters and the detector system are commonly used in both functions. The incident beam (I_0) is collimated by the collimator mirror and passed to the input polarizer (PL_{IN}) on the filter wheel through the blocking filters (BF#1 & #2). The input polarizer (PL_{IN}) produces linear polarization; the reflected component (I_r) goes into the interferometer and the transmitted component (I_t) is absorbed by a black wall. The linear polarized beam (I_r) is divided by the polarizing beam splitter (PL_{BS}), whose polarization angle is rotated by 45 degrees to the polarization angle of the incident beam. The two divided components ($I_{r\parallel}$ and $I_{r\perp}$) are reflected by roof-top mirrors; one is fixed and the other is movable to produce an optical path difference. Since the polarization angle of each component is rotated by 90 degrees by roof-top mirrors, the reflected component ($I_{r\parallel}$) is transmitted and the transmitted component ($I_{r\perp}$) is reflected by the beam splitter (PL_{BS}). The two interfering beams (I_{ri}) are modulated as an elliptical polarization and divided into two axis components by the output polarizer (PL_{OUT}) on the filter wheel, whose polarizing angle is the same with that of the input polarizer. The component

reflected by the output polarizer ($I_{ri\parallel}$) is focused on the LW detector through the low pass filter (WL) which covers the 55 – 90 cm⁻¹ wavenumber range (110 – 180 μm in wavelength), and the other component ($I_{ri\perp}$) is focused on the SW detector through the low pass filter (WS) which covers the 90 – 200 cm⁻¹ wavenumber range (50 – 110 μm in wavelength). The modulated powers on each detector ($I_{ri\parallel}$ and $I_{ri\perp}$) are described for incident photons of a wavenumber σ ,

$$I_{ri\parallel}(\sigma) = \frac{I_r}{2}(1 + \cos 2\pi\sigma x), I_{ri\perp}(\sigma) = \frac{I_r}{2}(1 - \cos 2\pi\sigma x) \quad (1)$$

where the x is the optical path difference. As shown in eq. (1), the polarities of the modulated signals are opposite each other.

To reduce the size of the optics, the incident angles of the polarizers are 30 and 60 degrees instead of the usual 45 degrees. All polarizers are wire grid type filters. The structure of the filters is thin copper wires printed on thin Mylar film mounted in a stainless frame. All optical filters used in the FIS-FTS are listed in table 1, which were supplied by QMC Ins. Ltd. As the result of the optical configuration of MPIs, only one fourth of the incident power is utilized for each detector for unpolarized incident flux, even in the ideal case. The actual optical efficiency is degraded by the quality of the optical components. Furthermore, the modulation efficiency depends on the optical alignment of the interferometer and on the detector properties. The performance of the FIS-FTS is described in section 4.

The FIS-FTS has two internal calibration sources; one consists of micro-lamps to monitor the detector responsivity and the other is a small blackbody source, whose temperature is controllable up to about 50K. The blackbody source is put at the input of the interferometer opposite to the input polarizer. The attenuation factor of the small blackbody source relative to the sky signal is about 10⁻³ due to its small aperture size of 0.7 mmφ. As the results of the small aperture size of the internal blackbody source, the effects of vignetting for pixels at the edge of the detector arrays and the modulation efficiency due to the misalignment of the two beams are smaller than for sky signals. Furthermore, the polarity of the blackbody interferograms is opposite to those for astronomical sources, since the transmitted beam is used for the internal blackbody source.

2.2. Mechanical Design

To realize the interferometer described above, the mechanical and thermal designs were optimized for the operation in space and cryogenic environment. The fundamental mechanical component of the interferometer is the mirror driving mechanism which produces the optical path difference between the two interfering beams. The driving mechanism for the FIS-FTS is based on the mechanism of the CIRS instrument on the Cassini spacecraft (Kunde et al. 1996). The roof-top mirror is mounted on a moving coil supported by four parallel tri-symmetrical leaf springs made of phosphor bronze, although the CIRS

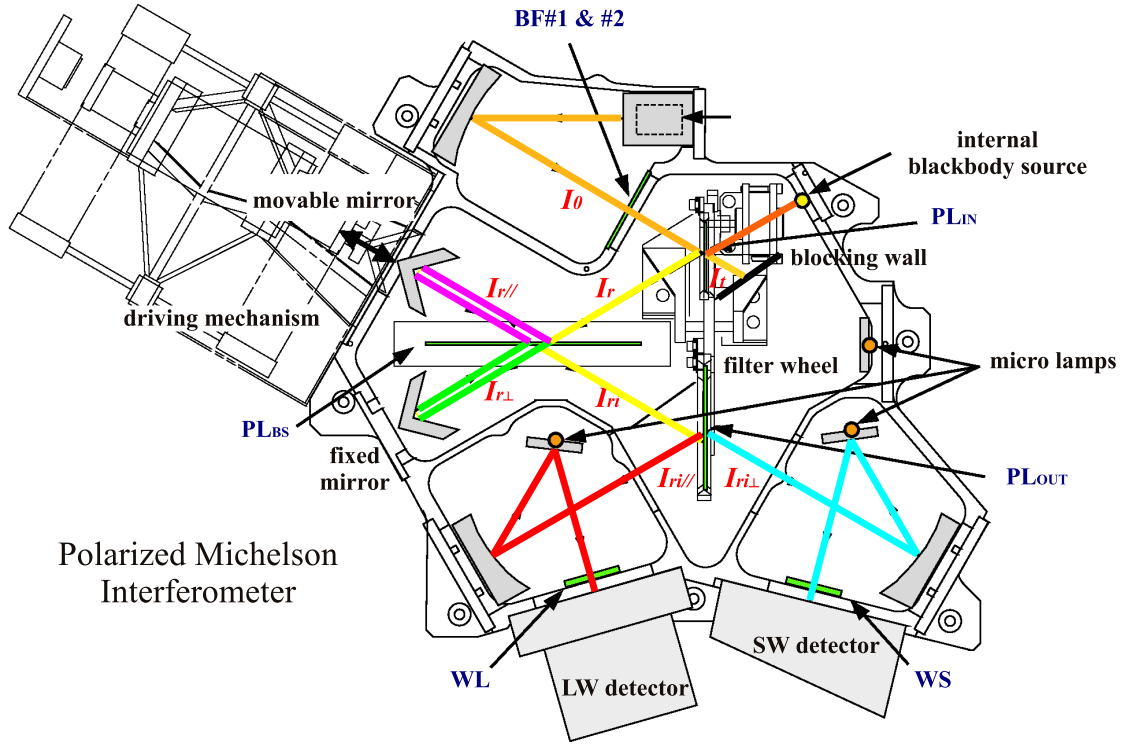


Fig. 1. Drawings of the FIS optical configuration. The major optical components are shown with labels. The FIS instrument provides two functions — the photometer (right side) and the spectrometer (left side), which use different optical paths. Each function is selected by rotating the filter wheel.

Table 1. Specifications of optical filters using in the FIS-FTS.

GROUP	NAME	TYPE	EFFECTIVE SIZE	PROPERTY
blocking filter	BF#1	multi mesh LPF	27 mm ϕ	$\sigma_{cut} = 430 \text{ cm}^{-1}$
	BF#2	multi mesh LPF	27 mm ϕ	$\sigma_{cut} = 300 \text{ cm}^{-1}$
polarizing filter	PL _{IN}	wire grid	30 mm ϕ	
	PL _{BS}	wire grid	85 mm ϕ	
	PL _{OUT}	wire grid	56 mm ϕ	
shaping filter	WS	multi mesh LPF	22 mm ϕ	$\sigma_{cut} = 218 \text{ cm}^{-1}$ (for SW)
	WL	multi mesh LPF	22 mm ϕ	$\sigma_{cut} = 90 \text{ cm}^{-1}$ (for LW)

Notes: All filters were supplied by QMC Instruments Ltd.

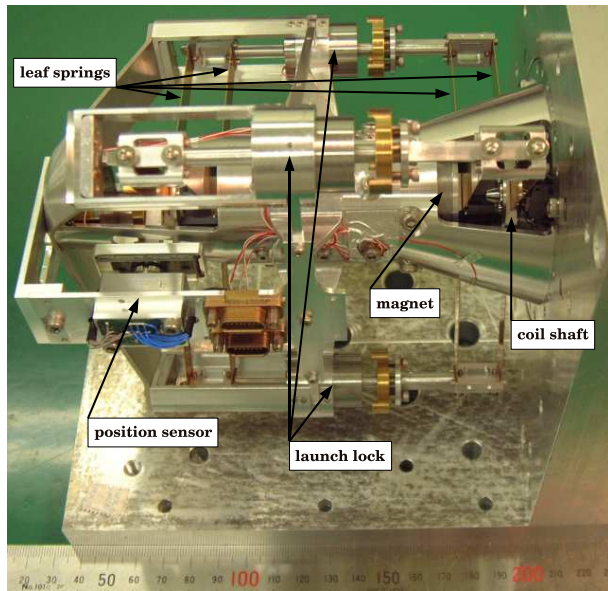


Fig. 2. A photograph of the mirror driving mechanism before installing on the FIS instrument. Optical shield is removed to see the inside of the mechanism.

adopts a moving magnet. The coil, made of superconducting wire to reduce power dissipation, is enclosed in a magnet made of rare earth metals, which is designed to optimize both of the magnetic field and weight. The driving mechanism of the FIS-FTS is shown in figure 2. The traveling length of the mirror driver is about ± 9.2 mm from the mechanical neutral position. The optical zero is set at the offset position about the half of the near side span. As the result of this configuration, the maximum optical path difference is about 27.6 mm (twice of 13.8 mm) and the shorter side is about 9.2 mm.

To measure the mirror position, a Heidenhain type optical scale is adopted. The optical scale and sensor optics used are from a commercial grade Heidenhain LIP-401P module. The sensor unit, however, is modified because the original module does not work at cryogenic temperatures. The resolution of the mirror position is $1 \mu\text{m}$ at ambient temperature (half of the scale pitch), corresponding to $2 \mu\text{m}$ in optical path difference. However, the actual step size is reduced at the operation temperature of about 3K, because of its thermal contraction. Since we did not calibrate the scale in laboratory, we have to calibrate the scale in space using well known astronomical lines. Unfortunately, we have no sensor to detect the optical zero position. The optical zero position must be determined from the interferograms themselves. The specifications of the mirror mechanism is summarized in table 2 with general properties of the FIS-FTS.

The mirror driving mechanism is quite fragile, because of its requirements of optical accuracy and high mobility to reduce power consumption. This is not a problem for operation in space, but is troublesome as a result of the strong vibrations experienced during the launch. To survive the launch, a launch lock mechanism was adopted

which fixes all movable parts by electromagnetic force during launch. The launch lock mechanism worked very well and the interferometer works as well in space as it did in the laboratory.

2.3. Detector System

The FIS-FTS is an imaging FTS incorporating two, two-dimensional detector arrays. The detectors for the FIS-FTS are common with the photometer of the FIS instrument. There are two sets of detector array, one is a monolithic Ge:Ga array which covers $90 - 200 \text{ cm}^{-1}$ ($50 - 110 \mu\text{m}$) (SW) (Fujiwara et al. 2003; Shirahata et al. 2004) and the other is a compact stressed Ge:Ga array for $55 - 90 \text{ cm}^{-1}$ ($110 - 180 \mu\text{m}$) (LW) (Doi et al. 2002). The readout method of both detectors is a Charge Trans-Impedance Amplifier (CTIA) realized by cryogenic Silicon MOS-FETs (Nagata et al. 2004). The CTIA integrates the photo-current of detector and is must be discharged periodically. The actual detector system has non-linearity due to the CTIA circuit itself, and additionally, the responsivity changes due to the drift of the effective detector bias voltage during the charge integration. Furthermore, extrinsic photoconductive detectors have a transient response with properties depending on both the background flux and the modulation amplitude (Kaneda et al. 2002). These properties of the detector system make it difficult to analyze the interferometer output. In particular, since FTSs measure the modulation of the signal in the time domain, understanding the detector transient response is critical. Effects of these properties on the interferograms and spectra are described later.

3. Operation

The FIS-FTS is operated in time domain. The moving mirror is controlled without mirror position feedback. That is, the mirror position is controlled by certain fixed pattern of the driving current. The driving current pattern is optimized to drive the mirror with constant speed. Sampling timing is also determined in the time domain and not in the optical phase domain. As a result, the sampling interval is not constant in optical path difference, but constant in time. The nominal mirror speed is nearly 0.08 cm sec^{-1} in optical path difference. The actual mirror speed has a global trend which is slower at the travel limits; the variation of the speed is less than $\pm 5\%$ across the whole travel span. The amplitude of the mirror speed fluctuation is also less than $\pm 5\%$ at the Nyquist sampling frequency without any disturbance. The normal sampling rate is nearly five times higher than the highest Nyquist frequency, which is helpful for reconstructing the interferograms from the integrated signal. After installing the FIS-FTS into the AKARI satellite, a mechanical interference between the mechanical cooler (Nakagawa et al. 2007) and the mirror driving mechanism was recognized. The driving speed is modulated by the 15 Hz drive frequency of the cooler, with an amplitude of about $\pm 25\%$ of the mirror speed, reduced to about $\pm 15\%$ in space. Since the interference frequency is almost out of

Table 2. Specifications of the FIS-FTS.

Imaging Fourier Transform Spectrometer for Far-Infrared Surveyor			
Optics	Polarized Michelson Interferometer		Martin-Puplett type
Mirror driving mechanism	leaf springs axis support with voice coil actuator		
Position Sensor	optical scale (2 μm in o.p.d.*)		no zero path detector
Spectral coverage	55 – 200 cm^{-1}		50 – 180 μm
Maximum o.p.d.* (L)	-0.9 – +2.8 cm		
Spectra resolution (1/2 L)	0.19 cm^{-1} (full res. mode)	1.2 cm^{-1} (SED mode)	without apodization
Mirror scan speed	$\sim 0.08 \text{ cm s}^{-1}$		
Detector system	2D photoconductive detector arrays with CTIAs [†]		
Detector unit name	SW	LW	
Detector type	monolithic Ge:Ga array	stressed Ge:Ga array	
Array format	3 × 20	3 × 15	
Pixel size	0.5 (0.55) mm	0.9 (1.0) mm	(pixel pitch)
Pixel FOV	26.8 × 26.8 arcsec ²	44.2 × 44.2 arcsec ²	
PSF [‡] (model)	$P_{FTS}(x, y) = P_{phot}(x - 7'', y) + P_{phot}(x + 7'', y)$; (x : major axis of array)		
FWHM	44'' / 39''	57'' / 53''	(major/minor)
Spectral coverage	85 – 200 cm^{-1}	55 – 90 cm^{-1}	
Sampling rate	85.336Hz	170.672Hz	

Notes.

* optical path difference

† Charge Trans-Impedance Amplifiers

‡ Point Spread Function for the photometer: $P_{phot} = \varepsilon e^{-(x^2+y^2)/2\sigma_1^2} + (1-\varepsilon)e^{-(x^2+y^2)/2\sigma_2^2}$; $\varepsilon = 0.8$; $\sigma_1 = 14.2''$; $\sigma_2 = 40.0''$ (for SW), $\varepsilon = 0.65$; $\sigma_1 = 17.0''$; $\sigma_2 = 46.5''$ (for LW)

the optical modulation frequency corresponding to the effective wavelength ($< 15\text{Hz}$), its influence can not be seen in spectra. The sampling timing and the mirror driving pattern are synchronized by the FIS-FTS controller. All pixel signals for each detector array are acquired at nearly the same time as the mirror position. The data reduction method of the FIS-FTS is described by Murakami et al. (2008).

For observation using the FIS-FTS, an astronomical observation template (AOT) is provided (see Kawada et al. (2007)), in which the calibration and the observation sequence are combined with some selectable parameters. Two driving current patterns are prepared for observations; one supports full travel span for high spectral resolution (full-res. mode) and the other reduces the span to one fourth but enables four times more scans (low-res. mode, which is called SED (Spectral Energy Distribution) mode). Driving speeds are almost the same in both modes.

4. Performances

4.1. Optical Performances

4.1.1. Modulation Efficiency

Optical performance of the interferometer is indicated by the modulation efficiency, which is defined as a ratio of the peak value of interferograms at the optical zero position to the constant signal level (constant part in eq. (1)). The modulation efficiency is primarily affected by two factors; filter properties and optical alignment.

Three polarizing filters are used in the FIS-FTS; all the

same type of wire grid filter. The polarizing efficiency was measured for each in the laboratory and is more than 90% for all. The resulting modulation efficiency due to the three polarizing filters in the MPIs configuration is about 80%. The misalignment of the polarization angle of three filters and ridge angle of roof-top mirrors reduce this efficiency. Since the misalignment of these angles was expected to be on the order of one degree, the effect of the misalignment to the modulation efficiency is negligible (less than 1%). A major factor affecting the modulation efficiency is the misalignment of optical axes of the two beams, which is generated by the roof-top mirrors. That is, the opening angle of the roof-top mirrors and the alignment of the tilt angle to the optical axis. The opening angle of the roof-top mirrors is less than one arcmin from 90 degrees, which was measured in the laboratory at cryogenic temperature. The remaining misalignment of two beams is due to the tilt of the roof-top mirrors. The misalignment of the two beam axes can be derived from the interferograms. If the tilting angles of the two roof-top mirrors are the same, the optical zero will appear at the same time for all pixels. The actual optical zero for each pixel, however, appear at different times; there is a delay along the major axis of the detector array. From the measurement of this delay, the displacement angle of the two roof-top mirrors could be estimated at about 3.5 arcmin in orbit, which corresponds to a misalignment of about 7 arcmin for the two beams. This value is consistent with the laboratory measurement, and means that there is no degradation in optical alignment due to the launch. The expected optical modulation efficiency was calculated for

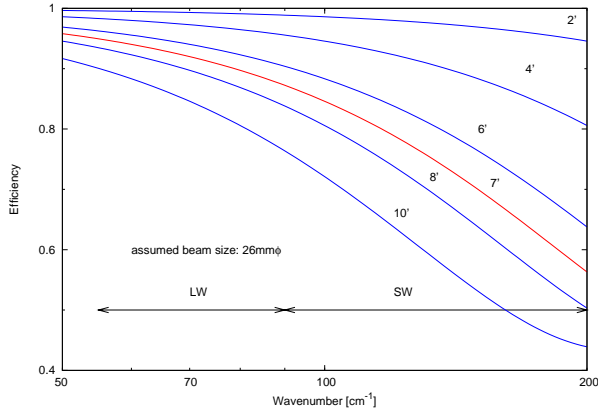


Fig. 3. Optical modulation efficiency expected as a function of misalignment of the two beams. Several cases of misalignment are calculated and the seven arcmin (red line) is the plausible case which is derived from the analysis of zero path positions (see text for details).

several degrees of misalignment. As shown in figure 3, the optical modulation efficiency due to the misalignment of two beams is about 95–85% for LW detector and about 85–60% for SW detector.

The modulation efficiency can be estimated from the measured signal ratio of the peak value of the interferogram at the optical zero to the DC value, which indicates the total incident power containing both coherent and incoherent components. Due to the transient response of the detectors, however, it is difficult to estimate the actual modulation efficiency from the interferograms. In section 5, we discuss the interferometric efficiency of the FIS-FTS estimated from the derived spectra, which include the detector transient response.

4.1.2. Image Quality

Image quality, which is a prominent feature of the FIS-FTS, was evaluated in orbit by observing Neptune with the FTS optics. The image of Neptune, which can be considered as a point source for the FIS instrument, was taken by a scanning observation mode. During the scanning observation, the movable mirror is in free motion away from the optical zero position (~ 0.9 cm in optical path difference). Neptune was observed with the same scanning mode with the photometer optics. The point spread functions (PSFs) of the photometer are well described by double Gaussian profiles, whose parameters are summarized in table 2. The resulting PSF of the FIS-FTS is rather broader than that of the photometer. The width of the PSF along the major axis of the detector array is wider, but there is no significant difference along the minor axis. This means that there is little affect on the image quality due to the FTS optics, i.e. the reflections at the surface of thin film polarizers. On the other hand, due to the misalignment of the roof-top mirrors, the image is elongated along the major axis of the detector. The elongated image of Neptune along the major axis of detector is consistent with an image derived from a beam misaligned by 7 arcmin, as described above. The imaging spectroscopic per-

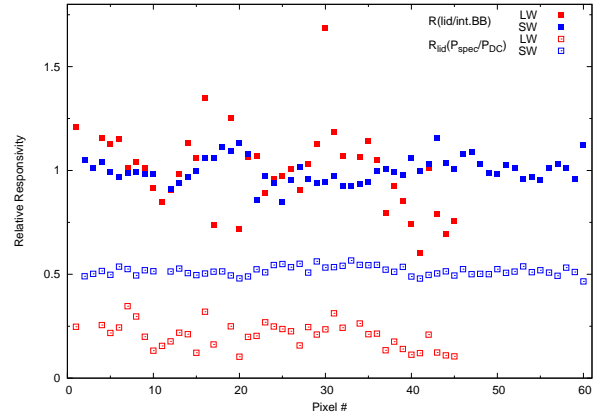


Fig. 4. The relative responsivity measured by telescope lid, which should be a flat source with temperature of 35K. The plot show the ratio of the integrated power of derived spectra of the lid to that of the internal blackbody source ($T=52$ K) or to that of the DC component. The ratio of the lid to the internal blackbody (filled square) indicate the no uniformity of the internal blackbody source primarily, though the ratio affected by the spectral response and the transient response of the detector. The ratios to the DC component (open square) indicates the interferometric efficiency, which includes the optical modulation efficiency and the detector transient effect. The plot of this value show wide variety from pixel to pixel, especially for the LW detector.

formance is demonstrated by observations of the Galactic center region (Yasuda et al. 2008), the star forming regions on the Galactic plane (Okada et al. 2008), and nearby galaxies (Takahashi et al. 2008).

The FIS-FTS measures a wide wavenumber region ($55 - 200$ cm^{-1}) at the same time with two kinds of detector array. To produce the whole spectrum of a sky position, we have to know the alignment of the field of views (FOVs) of two detector arrays. The alignment of two arrays was determined from scanning observations of point like sources. The FOVs of two detector arrays are not aligned well on the sky as shown in figure 3 in Kawada et al. (2007). The overlap region of the FOVs for the FIS-FTS is different from that of the FIS photometer, possibly arising from the alignment of the filter wheel. The smaller overlap region made it difficult to observe point like objects with both the arrays simultaneously.

Another factor affecting the image quality is a pixel-to-pixel variation in detector responsivity. During ground measurements of the instrument, the aperture lid of the cryostat was observed with the FIS-FTS as a flat source. The variations of the integrated signal power were about $\pm 30\%$ for the SW detector and $\pm 50\%$ for the LW detector, excluding a few extremely high pixels (see figure 4). Since pixels of the LW detector were made from discrete chips, in contrast to the monolithic array of the SW detector, it exhibits much larger variations in the integrated signal power, which is coupled with the variation of the spectral response of each pixel. In combination with the internal blackbody source, which is not a flat source due to the influence of the FIS-FTS optics, we expect to improve the

flatness of each detector to about $\pm 15\%$ and $\pm 30\%$ for the SW and LW detectors, respectively.

4.2. Performance as a Spectrometer

4.2.1. Distortion of Interferograms

An example of the detector signal is shown in figures 5(a) and 5(f). The output signal is an integration ramp curve with periodic resets due to the CTIA readout circuit. By differentiating the signal, a nominal interferogram including a DC component is derived (figures 5(b) and 5(g)). The periodic feature in the reset interval as mentioned in section 2.3 can be clearly seen. The periodic structure in the reset interval and random spikes due to cosmic ray hits must be removed. The standard data reduction flow for the FIS-FTS is described in Murakami et al. (2008). A typical FIS-FTS interferogram after processing by the standard data reduction tool is shown in figures 5(c) and 5(h). The left panels in figure 5 are plots of the LW detector (LW07) and the right panels are of the SW detector (SW32) using the internal blackbody source in the SED mode. This interferogram still has asymmetrical feature at the optical zero position, which can be clearly seen in the LW detector (figure 5(c)). The distortion of the interferogram comes from the detector transient response (time is from left to right in the figure). Due to the difference in the time constant between upward and downward signals, the baseline is decreasing near the optical zero position. The influence of the distortion of interferograms is discussed in next section.

4.2.2. Channel Fringes

As shown in figure 6, there is a strong fringe structure in both SW and LW signals, especially in the SW. A periodic structure can be seen in the SW interferogram with about ± 0.4 cm periodicity, occurring on both sides of the optical zero position (figure 6(a)). This fringe can be identified to the third order at least, and comes from multi-beam interference in the detector substrate, which is made of Ge crystal with 0.5 mm thickness. The optical path difference due to one reflection is $0.5 \text{ mm} \times 4$ (refraction index of Ge) $\times 2 = 4$ mm, and the actual value derived from the signal is 3.946 mm. The reflectivity estimated from the fringe contrast is about 0.4, which is consistent with reflectivity expected from the refractive index of Ge ($n = 4$).

Another type of channel fringe exists in the FIS-FTS, which can be clearly seen in the LW interferograms shown in figure 6(a). The first order of peaks appear on both sides of the main peak with about 0.8 cm separation in optical path difference. The corresponding fringe pitch in the spectra is about 1.21 cm^{-1} (figure 6(b)), with modulation amplitude significantly smaller than the other fringe seen in the SW spectrum. The observed fringes are nearly reproduced by a two parallel multi-reflection model with 4.1 mm gap and with about 20% reflectivity. A plausible explanation of this phenomena is the two blocking filters put on the optical path just after the collimator mirror (BF#1 & #2 in figure 1), with a physical gap of about 4 mm. The fact that this type of fringe can be seen in only sky signals, and not in the internal blackbody source, supports the multi-reflection model due to the blocking filters.

The reflectivity of 20%, however, is rather high compared to the laboratory measurements of the filters (about 10%). In SW detector spectrum, this type of fringe is not clear because the other fringe dominates, but it can be found in the SW interferograms.

As the result of the fringe structure, the spectral response of the FIS-FTS changes rapidly with frequency. It is important to correct the fringe structure to derive line intensities. Details of the treatment of the fringe in the data reduction are described in Murakami et al. (2008).

4.2.3. Spectral Resolution

The spectral resolution of the FIS-FTS is evaluated only in orbit using well known far-infrared lines of several sources. The expected spectral resolution from the maximum optical path difference ($L \sim 2.7$ cm) is about $1/2L \sim 0.19 \text{ cm}^{-1}$ (rectangle apodization) for the full-res. mode. Some fine structure lines, like [CII] (63.40 cm^{-1}), [NII] (82.10 cm^{-1}), [OIII] (113.18 cm^{-1}), are detected from many observations. An example of the detected lines is shown in figure 10 in Kawada et al. (2007), which is the [CII] line of the M82 galaxy. Physical line broadening of sources are negligible for the FIS-FTS because of its rather low spectral resolution ($R \sim 300$ at [CII] line). A spectral resolution derived from the observed lines is in good agreement with the expected value, which means the mirror driving mechanism works very well over the full travel span. There is no evidence of wavenumber and pixel position dependence to the spectral resolution. A wavenumber scale correction, however, is required for each pixel according to the actual optical path length, which is longer than scale length because of the off-axis beam. The maximum scale factor is expected to be less than 0.2%, for ideal, which is consistent with the observed trend.

4.3. Stability and Reproducibility

There are two types of internal calibration sources in the FIS-FTS: one is a micro lamp put in front of the detectors, the other is a small blackbody source put at the opposite port of the input polarizer. In the AOT of the FIS-FTS, the micro lamps are flashed at the beginning and end of each observation. The duration of each observation is about 30 minutes. The blackbody source is activated prior to observing the sky for about 7 minutes, with temperature fixed to about 38 K. Since the blackbody source is quite stable and reproducible, it can be used as the health check of the FIS-FTS.

In the one and half year lifetime of the AKARI cryogenics, the FIS-FTS has been operated for about 600 sets of pointed observations, corresponding to a total operation time of the FIS-FTS of about 200 hours. Using all observation data, we monitored the spectra of the internal blackbody source. Except for a few observations, which may be affected by radiation effects, the spectra of the internal blackbody source taken by the FIS-FTS are well reproducible within about $\pm 10\%$ variation. If the spectra are scaled with the integrated power of spectra, the variation of the spectra is reduced to less than $\pm 5\%$ for whole effective wavenumber region. The FIS-FTS system is quite stable and reproducible in spectra over the whole

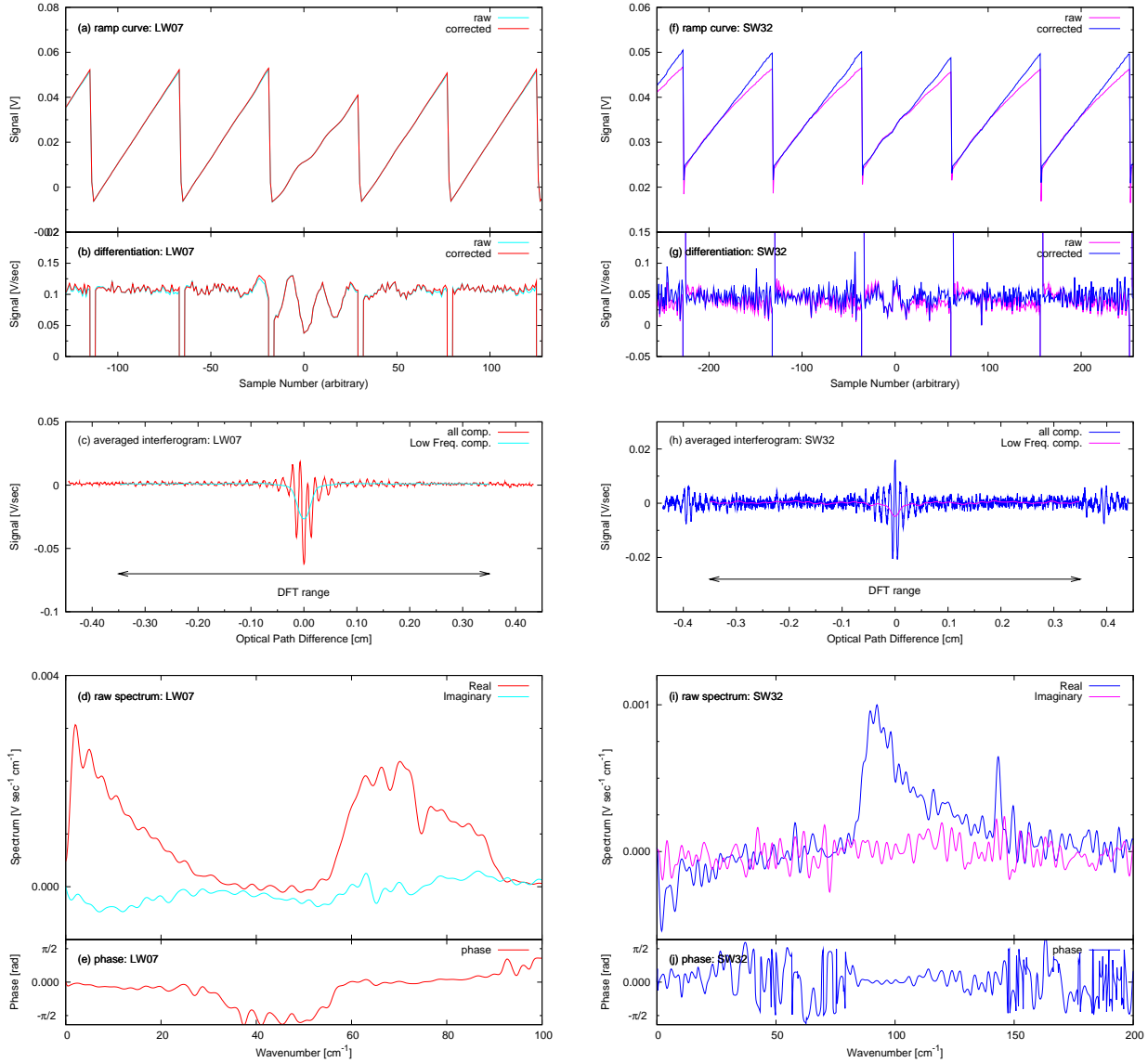


Fig. 5. An Example of the FIS-FTS signals, interferograms and spectra as an demonstration, which is measurement of the internal blackbody taken by the SED mode. The left panels are plots of the LW detector and the right panels are of the SW detector. Top panels (a) and (f) are raw signals of the LW07 and SW32 pixels, which are typical pixels of each detector. Panels of (b) and (g) show differentiations of raw signal in time domain. The corrected signals of the non-linearity related to the readout electronics are also plotted on the raw signals. The middle panels (c) and (h) indicate the averaged interferograms of twelve scans (for same scan direction). The bottom panels (d) and (i) show raw spectra of the interferograms shown in (c) and (h). Both real and imaginary part are plotted, and the phase signal are indicated in (e) and (j). Low frequency structures appeared in (d) and (i) come from the distortion of the interferograms. The contribution of low frequency components ($< 50 \text{ cm}^{-1}$) are plotted on the interferograms (c) and (h), which are derived by the inverse Fourier transformation.

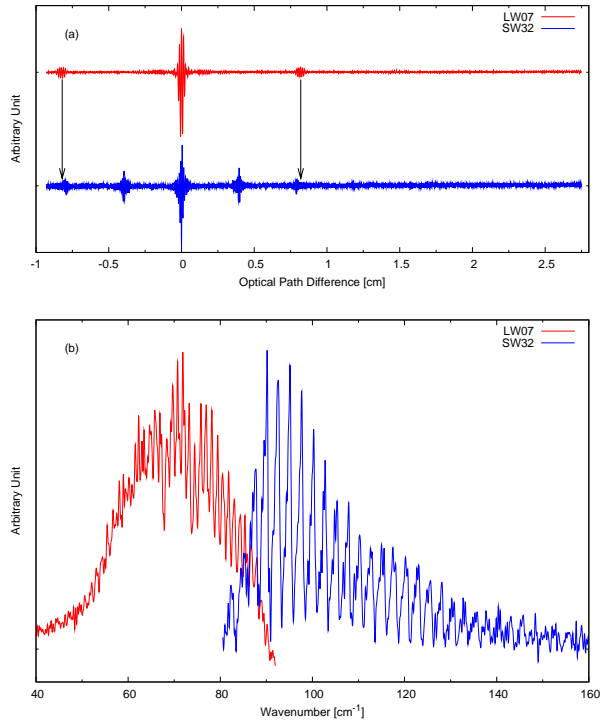


Fig. 6. An example of spectra taken by the full res. mode, which are spectra of the telescope lid. The top panel (a) shows interferograms averaging 6 scans of same scanning direction. There are sub-structures in the interferograms. The upper interferogram is of LW07, and the lower one is of SW32. In the SW32 interferogram, same sub-feature seen in the LW07 can be recognized adding to the own periodic sub-structures. The bottom panel (b) indicates the Fourier transformed spectra of the interferograms in the top panel. There are fringe structures in both SW and LW spectra, whose periods are different from each other.

observation period.

The FIS-FTS covers a wide wavenumber region with two kinds of detector arrays. To get the whole spectrum, we must combine two spectra taken by both detector arrays. The effective wavenumber overlap of the two detector arrays is around $85 - 90 \text{ cm}^{-1}$, which is helpful to check the reproducibility of the spectra for both detector arrays.

5. Discussions

The overall spectral response of the FIS-FTS is determined by three factors, mainly; the filter transmission including multi-beam interference, the modulation efficiency due to the optical alignment, and the detector spectral response including the multi-beam reflections. In addition to the optical response, the transient response of the photoconductive detectors affects the resulting spectra through the distortion of the interferograms. In this section, we discuss about the performance as the FTS with photoconductive detectors.

The fringe structure in the spectra complicates derivation of line intensities. Though the multiple reflections

in the substrate of the SW detector contribute to the improvement of the total responsivity, the multi-beam interference fringes make it difficult to measure the spectra. The fringes could be modeled by multi-beam interference of the detector substrate or two parallel blocking filters. The actual fringe shape is, however, different from an ideal Airy function with proper parameters. It may be effects of the convergent beam or imperfect parallelism of the two flat surfaces. In practice, correction using templates made from actual data are effective. The continuum spectra derived from the short range interferograms are equal to the smoothed spectra with high resolution. If the responsivity at the line center is higher than the smoothed responsivity, a line to continuum ratio should be an overestimation, and vice versa. The data analysis and calibration methods are discussed in detail by Murakami et al. (2008).

The FIS-FTS is the first FTS operating with an extrinsic photoconductive detector in space. As shown in figure 5, interferograms are distorted by the detector transient response. As the result of the distorted interferogram, the spectrum has a prominent structure at lower frequency as shown in figure 5(d)(i). The low frequency component comes from the bump in the baseline around the optical zero position. It can be clearly seen as the inverse Fourier transform of the low frequency component (see figure 5(c)(h)). For the nominal operation of the FIS-FTS, the effective wavenumber ranges correspond to the modulation frequency ranges of 3.5 - 7 Hz and 7 - 15 Hz for the LW detector and the SW detector, respectively. As shown in figure 5(d)(i), which are the data of LW07 and SW32 pixels, the real spectrum may be isolated from the low frequency component, which comes from the detector transient response artifact. The influence of the detector transient effect on the spectra are different from pixel to pixel. The LW detector has an especially wide variation in the transient response from pixel to pixel. Therefore, the distortion of the real spectrum by the detector transient effect should be evaluated carefully for precise analysis. In the zero order analysis, however, it may be acceptable to ignore the detector transient effects. The calibration strategy and accuracy of the FIS-FTS are discussed in Murakami et al. (2008).

We can derive the interferometric efficiency by comparing the integrated power of the spectrum in the effective wavenumber range with the incident power. The overall efficiencies are around 50% and 20% for SW and LW detectors, respectively (open squares in figure 4). Considering the optical modulation efficiency (see 4.1.1), the degradation factors due to the detector transient response are ~ 0.7 and ~ 0.25 for SW and LW detectors, respectively. In a future paper, we will discuss the correction of the interferograms in the time domain considering the physical model of the photoconductive detector response. The operation of the FIS-FTS, unfortunately, was not optimized for photoconductive detectors because of our poor experience of FTS with photoconductive detectors. For future missions, such as SPICA which is the large infrared telescope mission (Nakagawa & Murakami 2007), a FTS with photoconductive detectors is one of the possible choices

for a high performance spectrometer. To bring out the maximum performance, we have to study the FTS with photoconductive detectors and a proper physical model of the photoconductive detector. The data produced by the FIS-FTS are quite valuable for this purpose as a precursor mission.

6. Summary

The FIS-FTS instrument is the first imaging Fourier transform spectrometer for far-infrared astronomy operated in space. The FIS-FTS was installed as a function of the Far-Infrared Surveyor (FIS) on the AKARI satellite, which was launched on February 21, 2006 (UT). All functions of the FIS-FTS worked in orbit as well as they did in the laboratory. The performance of the FIS-FTS also achieved the same level seen in the laboratory. During the one and half year lifetime of the FIS instrument, the total operation time reached more than 200 hours or about 600 sets of pointed observations. The sensitivity, spectral response and resolution are quite stable for all observations.

A unique feature of the FIS-FTS is the detector system; it is the first case to adopt a photoconductive detector array to FTSS. Photoconductive detectors have high responsivity on one side, but severe transient response effect on the other side. As the result of this combination, the interferograms taken by the FIS-FTS are distorted and the spectra are affected by the transient response of the detectors. These difficulties in measuring the spectra should be avoided or reduced in future missions, if adopting a FTS with photoconductive detectors. The FIS-FTS provides good data for studying the detector transient effects on FTSS.

The AKARI project, previously named ASTRO-F, is managed and operated by the Institute of Space and Astronautical Science (ISAS) of Japan Aerospace Exploration Agency (JAXA) in collaboration with groups in universities and research institutes in Japan, the European Space Agency, and Korea. We thank all the members of the AKARI/ASTRO-F project for their continuous help and support. FIS was developed in collaboration with Nagoya University, ISAS, University of Tokyo, National Institute of Information and Communications Technology (NICT), National Astronomical Observatory of Japan (NAOJ), and other research institutes. Optical design of the FIS-FTS was done with the help of JASCO, and mechanical design was done with the Technical Center of Nagoya University. QMC Instruments Ltd developed optical filters for the FIS instrument. Many graduate students, especially Mr. Yasushi Tsuzuku, Mr. Yoshikazu Kuwata, Mr. Hiroshi Utsuno, Mr. Keita Ozawa and Mr. Tetsuo Imamura, worked for development, fabrication and testing of the FIS-FTS. We thank all the members related to the FIS-FTS for their intensive efforts. We really appreciate the useful advice on FTSS from Prof. Donald E. Jennings at NASA/Goddard Space Flight Center. We would like to thank Prof. Annie Zavagno and Dr. Jean-Paul Baluteau at the Laboratoire d'Astrophysique de

Marseille in France, Peter Davis at Blue Sky Spectroscopy in Canada, and Prof. David Naylor and Brad Gom at the University of Lethbridge in Canada for their contributions to the FIS-FTS data reduction and valuable discussions.

References

- Doi, Y. et al. 2002, *Adv. Space Res.*, 30, 2099–2104
 Fujiwara, M., Hirao, T., Kawada, M., Shibai, H., Matsuura, S., Kaneda, H., Patrashin, M. A., & Nakagawa, T. 2003, *Appl. Opt.*, 42, 2166–2173
 Hirao, T., Matsumoto, T., Sato, S., Ganga, K., Lange, A. E., Smith, B. J., & Freund, M. 1996, *PASJ*, 48, L77–L82
 Kaneda, H., Okamura, Y., Nakagawa, T., & Shibai, H. 2002, *Adv. Space Res.*, 30, 2105–2110
 Kaneda, H., Kim, W., Onaka, T., Wada, T., Ita, Y., Sakon, I., & Takagi, T. 2007, *PASJ*, 59, 423–427
 Kawada, M. et al. 2007, *PASJ*, 59, 389–400
 Kessler, M. F. et al. 1996, *A&A*, 315, L27–L31
 Kessler, M. F. 2002, *Adv. Space Res.*, 30, 1957–1965
 Kunde, V. G. et al. 1996, *Proc. SPIE*, 2803, Ed. L. Horn, 162–177
 Martin, D. H., & Pulett, E. 1969, *Infrared Phys.*, 10, 105
 Mather, J. C. 1993, *Proc. SPIE*, 2019, Ed. M. S. Scholl, 146–157
 Mather, J. C., Fixsen, D. J., & Shafer, R. A. 1993, *Proc. SPIE*, 2019, Ed. M. S. Scholl, 168–179
 Murakami, H. et al. 1996, *PASJ*, 48, L41–L46
 Murakami, H. et al. 2007, *PASJ*, 59, 369–376
 Murakami, N. et al. 2008, *PASJ*, XX, XXX–XXX
 Nagata H., Shibai H., Hirao T., Watabe T., Noda M., Hibi Y., Kawada M., & Nakagawa T. 2004, *IEEE Trans. Elec. Devices*, 51, 270
 Nakagawa, T., et al. 2007, *PASJ*, 59, 377–387
 Nakagawa, T., & Murakami, H. 2007, *Adv. Space Res.*, 40, 679–683
 Neugebauer, G. et al. 1984, *ApJ*, 278, L1–L6
 Ohyama, Y. et al. 2007, *PASJ*, 59, 411–422
 Okada, Y. et al. 2008, in preparation
 Onaka, T., Yamamura, I., Tanabe, T., Roellig, T. L., & Yuen, L. 1996, *PASJ*, 48, L59–L63
 Onaka, T. et al. 2007, *PASJ*, 59, 401–410
 Shibai, H., Okuda, H., Nakagawa, T., Makiuti, S., Matsuhara, H., Hiromoto, N., & Okumura, K. 1996, *PASJ*, 48, L127–L131
 Shirahata, M. et al. 2004, *Proc. SPIE*, 5487, Ed. J. C. Mather, 369–380
 Takahashi, H., Kawada, M., Murakami, N., Ozawa, K., Shibai, H., & Nakagawa, T. 2003, *Proc. SPIE*, 4850, Ed. J. C. Mather, 191–201
 Takahashi, H. et al. 2008, in preparation
 Tanaka, M., Matsumoto, T., Murakami, H., Kawada, M., Noda, M., & Matsuura, S. 1996, *PASJ*, 48, L53–L57
 Werner, M. W. et al. 2004, *ApJS*, 154, 1–9
 Yasuda, A. et al. 2008, in preparation